

Large-scale Coronal Propagating Fronts in Solar Eruptions as Observed by the Atmospheric Imaging Assembly on Board the Solar Dynamics Observatory – An Ensemble Study

Nariaki V. Nitta¹, Carolus J. Schrijver¹, Alan M. Title¹ and Wei Liu^{1,2}

Abstract

This paper presents a study of a large sample of global disturbances in the solar corona with characteristic propagating fronts as intensity enhancement, similar to the phenomena that have often been referred to as EIT waves or EUV waves. Now Extreme Ultraviolet (EUV) images obtained by the *Atmospheric Imaging Assembly* (AIA) on board the *Solar Dynamics Observatory* (SDO) provide a significantly improved view of these large-scale coronal propagating fronts (LCPFs). Between April 2010 and January 2013, a total of 171 LCPFs have been identified through visual inspection of AIA images in the 193 Å channel. Here we focus on the 138 LCPFs that are seen to propagate across the solar disk, first studying how they are associated with flares, coronal mass ejections (CMEs) and type II radio bursts. We measure the speed of the LCPF in various directions until it is clearly altered by active regions or coronal holes. The highest speed is extracted for each LCPF. It is often considerably higher than EIT waves. We do not find a pattern where faster LCPFs decelerate and slow LCPFs accelerate. Furthermore, the speeds are not strongly correlated with the flare intensity or CME magnitude, nor do they show an association with type II bursts. We do not find a good correlation either between the speeds of LCPFs and CMEs in a subset of 86 LCPFs observed by one or both of the *Solar and Terrestrial Relations Observatory* (STEREO) spacecraft as limb events.

Subject headings: Sun: corona – Sun: coronal mass ejections (CMEs) – Sun: flares – Sun: oscillations - Sun: UV radiation

¹Lockheed Martin Advanced Technology Center, Dept/A021S, B/252, 3251 Hanover Street, Palo Alto, CA 94304, USA

²W. W. Hansen Experimental Physics Laboratory, Stanford University, Stanford, CA 94305, USA

1. Introduction

The so-called EIT wave¹ (Moses et al. 1997; Thompson et al. 1998) is a propagating intensity enhancement in coronal EUV lines, notably in Fe XII lines around 195 Å at ≈ 1.5 MK. Its discovery by the *Extreme Ultraviolet Imaging Telescope* (EIT; Delaboudinière et al. 1995) on board the *Solar and Heliospheric Observatory* (SOHO) sparked renewed interest in global disturbances that had been associated with solar flares. The most typical example of such disturbances is the Moreton-Ramsey wave in H α images (Moreton & Ramsey 1960). Uchida (1968) modeled Moreton-Ramsey waves as chromospheric intersections of flare-launched fast-mode MHD waves in the corona, where the magnetoacoustic speed is an order of 1000 km s^{-1} , comparable to the typical speed of Moreton-Ramsey waves. The same fast-mode MHD waves may be responsible for metric type II radio bursts and filament oscillations that had been found even earlier.

EIT waves were initially thought to be the coronal counterparts of Moreton-Ramsey waves (e.g., Thompson et al. 1999). However, this idea started to be questioned. First, the typical speed of EIT waves ($200\text{--}400 \text{ km s}^{-1}$, see Thompson & Myers 2009) is much lower than that of Moreton-Ramsey waves. A magnetoacoustic speed that matches the EIT wave initially implied a high plasma β (Wang 2000; Wu et al. 2001), not usually applicable in the low corona, although later works (Ofman & Thompson 2002; Wu et al. 2005; Schmidt & Ofman 2010; Downs et al. 2011) have shown that this is not always the case. Second, EIT waves are more intimately associated with coronal mass ejections (CMEs) than with flares (Biesecker et al. 2002; Cliver et al. 2005; Chen 2006), whereas the MHD waves responsible for Moreton-Ramsey waves are often attributed to flares as were in Uchida’s original concept in the pre-CME era. Third, some of the reported EIT waves appear to represent stationary brightening (Delannée & Aulanier 1999).

One way of interpreting these properties of EIT waves is that they are not fast-mode MHD waves, but that they are signatures more directly related to CMEs. They include current shells (Delannée & Aulanier 1999), stretched CME loops (Chen et al. 2002), and reconnection of CMEs with quiet-Sun bipoles (Attrill et al. 2007). Furthermore, slow mode waves (Wang et al. 2009) and solitons (Wills-Davey et al. 2007) were also proposed as contributors to EIT waves.

However, it is still more common to interpret EIT waves in terms real waves, fast-mode MHD waves in particular. In certain events observed in H α , soft X-rays, He I λ 10830

¹It is also referred to as the EUV wave to remove the dependency on the instrument. For clarity, however, we simply use the EIT wave throughout the paper.

and radio (at both microwave and metric wavelengths), the tracks of the EIT wave fronts are found to be consistent with flare-generated large-amplitude MHD waves that undergo deceleration (Warmuth et al. 2001, 2004; Vršnak et al. 2006). Other characteristics that support the wave nature of EIT waves include the fronts that decelerate (Long et al. 2011a), broaden and decrease in amplitude with time (Veronig et al. 2010), and deflect at coronal hole boundaries (Gopalswamy et al. 2009).

It appears that the lack of a consensus view of the EIT wave is due partly to the lack of its definition beyond “the outermost propagating intensity front reaching global scales” (Patsourakos & Vourlidas 2012). Another major factor is the 10–20 minute cadence of EIT, which likely failed to capture the early phase of many events, where the speed may have been higher. Indeed, higher speeds and decelerating profiles were obtained using data from the *Extreme Ultraviolet Imager* (EUVI; Howard et al. 2008; Wuelser et al. 2004) on the *Solar Terrestrial Relations Observatory* (STEREO), which have slightly better cadence (see Long et al. 2008, 2011a). Note, however, that the maximum speed found by Long et al. was only 475 km s^{-1} partly because of solar minimum conditions (see Nitta et al. 2013, for an extensive list of EIT waves observed by EUVI during 2007–2009). Despite the problems arising from the low cadence, our knowledge of EIT waves is still built heavily on a limited set of EIT observations, especially on the list of events during March 1997–June 1998 as compiled by Thompson & Myers (2009).

One remarkable departure in recent years, however, is a growing recognition that EIT waves could contain both wave and CME-related components as first pointed out by Zhukov & Auchère (2004)². Interestingly, this change of our perception is driven by advanced 3d MHD numerical simulations for a few events (Cohen et al. 2009; Downs et al. 2011, 2012) rather more than by observations.

Observationally, it is clear that a breakthrough in understanding global coronal disturbances, EIT waves included, should come with the *Atmospheric Imaging Assembly* (AIA; Lemen et al. 2012) on board the *Solar Dynamics Observatory*, which provides uninterrupted full disk images with unprecedented high cadence, high sensitivity and broad temperature coverage. Already more than 30 papers using AIA data have been published that include discussions of EIT waves, delivering some promising results. However, almost all the published papers on EIT waves using AIA data have so far been case studies of one or a few events, not answering how special they are, reflecting their specific processes or conditions.

²It is fair to mention that the co-existence of the wave and CME-related components was first shown by Chen et al. (2002) in their 2d MHD simulations of eruptions. However, these authors associated EIT waves exclusively with the CME-stretched loops.

In this paper, we take a complementary approach of studying a large sample of events that look like EIT waves in AIA images, and focus on their speeds. This is motivated primarily by the recent attempt of distinguishing three populations of EIT waves on the basis of their kinematic behaviors (Warmuth & Mann 2011). According to Warmuth & Mann, fast and decelerating EIT waves may correspond to non-linear fast-mode MHD waves (shocks), and those with moderate and constant speeds to linear fast-mode MHD waves propagating at the local fast-mode speed. The slowest EIT waves may correspond to CME-related magnetic reconfiguration. After studying similar phenomena in AIA data, however, it appears that EIT observations did not capture the full range of global disturbances in the corona largely because of the poor cadence. With AIA, we can more clearly observe how they propagate in short time intervals that used to be covered by less than a few EIT images. It is likely that we now deal with phenomena not adequately represented by “EIT waves.” Therefore in this paper we use the term “Large-scale Coronal Propagating Fronts” (LCPFs) to refer to EIT-wave-like phenomena, as temporally resolved in AIA data. §2 describes how we find LCPFs and maintain a catalog. In §3 we discuss how LCPFs are associated with other solar transient phenomena. We discuss the propagation speeds of LCPFs in §4. The implications of this study are discussed in §4.

2. A Catalog of LCPFs

We have found 171 LCPFs during April 2010–January 2013. As of this writing, the software to automatically detect and characterize EIT waves has not yet been implemented in AIA data pipeline as part of the Computer Vision for the SDO (cf. Martens et al. 2012). Therefore we basically need to rely on visual inspection of images to find LCPFs. As a first step, we review running difference images in 211 Å, 193 Å, and 171 Å channels at a sampling of every five minutes, using a high-performance image-viewing tool called Panorama (Hurlburt et al. 2012). This exercise results in more than 200 candidates of LCPFs. In the absence of a universal and quantitative definition of EIT waves, our working definition of LCPFs is that they need to exhibit an angular expanse of $\gtrsim 45^\circ$ and to propagate at least 200 Mm away from the center of the associated eruption. For each of the candidates, we measure the width and distance of the front in the last 193 Å difference image on which it can be traced. We use EUVI 195 Å images to measure the width and distance of the front that comes from a region close to the limb and propagates predominantly along the limb, leaving almost negligible signatures on disk. For the period of interest, limb events from Earth are typically viewed as disk events by one or both of the STEREO spacecraft. After dropping the candidates that do not meet the above criteria, we are left with 171 LCPFs. They are listed in Table 1.

In order to study the global properties of LCPFs such as their relations with CMEs, we need to analyze full-disk images. Considering our event sample size, it is not realistic at the moment to conduct an analysis in the full-resolution images of 4096^2 pixels. Thus they are rebinned to 1024^2 pixels for the present work. Our experiences have shown that movies of co-aligned images are extremely useful for following the spatio-temporal variations of dynamic phenomena on the Sun. Therefore, for each LCPF, we make standard SolarSoft movies (Javascript and MPEG) in AIA’s seven EUV channels and three formats (intensity, running difference and base difference). Additionally, to benefit from stereoscopic views, two other sets of movies are made of AIA 193 Å and STEREO-A or -B EUVI 195 Å pairs. It is also important to follow LCPFs with respect to the development of the associated flares as captured in soft X-ray light curves. To accommodate GOES soft X-ray light curves in the movies, we further shrink the images to 768^2 pixels, although images of 1024^2 pixels are used when measuring LCPFs (§4). LCPFs are usually found in running difference movies, but base difference movies are useful for isolating long-lasting dimming, which may correlate with the spatial extent of the CME (Thompson et al. 2000a). Intensity movies, in which strong LCPFs are visible, also help us locate coronal holes and active regions that deflect LCPFs. The catalog of LCPFs with all these movies are online at http://aia.lmsal.com/AIA_Waves/index.html, which may contain more events over time that are not used in the present study.

Out of the 171 LCPFs, 138 are seen to propagate across the solar disk, and 22 (mostly from regions close to the limb) to propagate predominantly over the limb without clear fronts on disk. The remaining 11 events do not show a clear front in either way, although future image processing techniques may restore it. In the following sections, even though a number of recent studies have examined propagations over the limb (e.g., Downs et al. 2012; Liu et al. 2012), our emphasis here is on the first category, since many scientists may have associated EIT waves with circular fronts propagating across the disk.

3. Association of LCPFs with other observables

We study the association of the 138 LCPFs that propagate across the solar disk with solar flares, CMEs and type II radio bursts, following a past study by Biesecker et al. (2002) for the EIT waves that were compiled by Thompson & Myers (2009). In Table 1, they are given in the third, ninth and tenth columns. The GOES X-ray peak flux of the associated flares and the presence of type II bursts are easily available from NOAA lists or SolarSoft distributions. However, the same may not apply to CMEs because the online CME catalogs tend to contain as many events as possible, some of which may be too insignificant to qualify as CMEs. Rather than simply showing whether the LCPF is associated with a CME as

found close in time in a catalog, we differentiate the significance of CMEs or outflows into four levels similar to the flare magnitude which is often referred to as X-class and so on. By examining the available coronagraph data (COR-1 and COR-2 on STEREO and LASCO on SOHO), we introduce the following CME levels; (1) Weak outflow that becomes invisible before the heliocentric distance of $5 R_{\odot}$, (2) Narrow ($<60^{\circ}$) or slow ($<500 \text{ km s}^{-1}$) outflow traceable beyond $5 R_{\odot}$, but typically not being reminiscent of the three-part CME structure, (3) Well-formed CME, fast and wide, with a flux rope or three-part structure, (4) Similar to level 3, but very fast ($>1500 \text{ km s}^{-1}$).

Separating the CMEs into groups may not be done completely objectively, which is especially true for the distinction between CMEs of levels 3 and 4, as many different threshold speeds could be considered. Nevertheless, we consider a grouping like this to be important when we understand how LCPFs arise in the overall picture of sudden energy release in the solar corona. Patsourakos & Vourlidas (2009) criticized careless use of the term ‘‘CME’’ to include coronal structures that are not part of the flux rope. Here we propose that how far it can travel may be another criterion for a CME.

Table 2 shows the breakdown into the flare class of the CME levels defined in this way and the presence/absence of a type II burst. Flares whose peak flux is $<10^{-6} \text{ W m}^{-2}$ are labeled ‘‘<C.’’ To our surprise, more than 1/3 of our LCPFs belong to CME level 1, given the strong correlation of EIT waves with CMEs as widely accepted (Biesecker et al. 2002; Cliver et al. 2005; Chen 2006). Although we observe at least a minor outflow in the coronagraph data of almost all of our LCPFs, many of them may not be real CMEs defined as ejections of coronal magnetized plasma into the heliosphere.

4. Speeds of LCPFs

The speeds of the 138 LCPFs that propagate across the disk are measured in 193 Å images (Figure 1), using a semi-automated scheme. As the first step, we de-rotate the images to a reference time in order to compensate for differential solar rotation, using the standard SolarSoft routine `drot_map.pro`. The reference time is typically set to be 5–10 minutes before the onset of the associated flare. Then, as explained in Liu et al. (2010), we follow a technique that is widely used for tracing waves (see, for example, Podladchikova & Berghmans 2005, who developed the Novel EIT Wave Machine Observing (NEMO) code). First, the eruption center is identified as a pole. Here we make 24 equally spaced longitude sectors from the pole that are 15° wide. For each sector the intensity profile is obtained as a function of the distance along the longitude, by averaging pixels in the latitudinal direction. This corrects for the curvature of the solar surface. Such a profile is obtained at the cadence of

12 s (or 24 s after October 2010³). The images with automatic exposure control are excluded to avoid spurious effects in difference images irrespective of which events we deal with.

We now have a 2d array of intensity as a function of both time and distance from the eruption center. This should contain useful information on the front such as the amplitude and width (Veronig et al. 2010; Liu et al. 2010). However, extraction of such information may not be straightforward on a large sample, because it can be affected by local conditions specific to individual events. In this paper we instead concentrate on the simplest quantity, namely the propagation speed, which is measured on a distance-time plot. In Figure 1, we show distance-time plots for all the sectors as running difference images, on which LCPFs appear as bright ridges. We also include the normalized GOES 1–8 Å soft X-ray flux as plotted on the same time axis.

For each sector, we calculate the speed and acceleration by fitting first- and second-order polynomials to the front edge of the most prominent ridge in the distance-time plot. MPFIT (Markwardt 2009) is used to calculate these parameters with error bars, assuming a uniform uncertainty of 5 Mm in locating the front. This is done only in the distance range until the propagation is clearly altered by active regions or coronal holes. Beyond this range, the technique may not make sense because we are probably not tracing the same front. Furthermore, the technique may not work as well in data whose temporal resolution is much worse than that of AIA (e.g., Nitta et al. 2013). In intensity images (not shown), active regions are seen in the sectors 1–3, 6, 7, 10, 11, 21, 23 and 24 and coronal holes in sectors 12–17, where the main ridge shows clear deceleration. We examine the distance-time plot in each sector and select the one with the highest speed, making sure not to select a sector in which the measurement is too susceptible to foreshortening toward the limb. In this case sector 4 is selected, and the speed measured in that sector is registered as the speed of this LCPF (see the sixth and seventh columns in Table 1).

Figure 2 shows distance-time plots from images in 171 Å. Generally, the fronts are harder to trace. Moreover, they appear as depression in several sectors rather than as intensity enhancement. This may indicate heating at the fronts (Wills-Davey & Thompson 1999; Schrijver et al. 2011; Liu et al. 2012), for example, from $\lesssim 1$ MK to ≈ 1.5 MK. In this example, the front in sector 4 still appears as intensity enhancement. The eighth column in Table 1 shows the appearance of the front in 171 Å channel, summarized in the last three columns in Table 2. In 171 Å images, 42% of LCPFs are not clearly seen (below the

³Then the automatic exposure control (AEC) was implemented on every other EUV image to reduce the effect of saturation in flare images. To produce difference images unaffected by the spurious effects arising from different exposure times, we use only AEC-off images.

noise level) in the sector of the fastest front at 193 Å and another 42% are seen as intensity depression.

Let us discuss the 22 LCPFs that propagate predominantly over the limb. We measure their speeds along the limb at the heliocentric distance of $1.15 R_{\odot}$ (see Patsourakos et al. 2009; Kienreich et al. 2009, for stereoscopic determination of the height of EIT waves), as shown in Figure 3. In Figure 4, they are compared with the speeds measured in EUVI 195 Å images of the same LCPFs in the same directions (north or south) viewed as disk events. The error bars for the speeds from AIA are based on the uniform uncertainty of locating the front to 5 Mm. It is more difficult to measure the speeds of faster LCPFs in EUVI data, given the 2.5–5 m cadence. Therefore the error bars for the speeds from EUVI are essentially proportional to the speeds with other corrections due to the cadence and the visibility of the fronts, which may be still tentative. Irrespective of the error bars, Figure 4 indicates that the two speeds are not well correlated. In many events, the AIA speed is higher than the EUVI speed, presumably reflecting the difference in the cadence (cf. Long et al. 2008, 2011a). But other LCPFs show the opposite trend, suggesting that the limb view of LCPFs after all reflect line-of-sight integration of the fronts whose propagations may not only be in the north-south directions but also in other directions. Although it may be worthwhile to investigate reasons (e.g., projection effect) for the discrepancy of the speeds in individual cases, we generally argue that these events may not be directly comparable to the LCPFs that are seen to propagate across the solar disk in AIA images.

For the 138 LCPFs that are seen to propagate across the solar disk, we get $v_{\text{mean}}=644 \text{ km s}^{-1}$ and $v_{\text{median}}=607 \text{ km s}^{-1}$, which are much higher than the typical speed of EIT waves (200–400 km s^{-1} , see Thompson & Myers 2009). Figure 5 shows the speed vs acceleration of these LCPFs. Up to $v \approx 800 \text{ km s}^{-1}$, there may be a weak trend of faster LCPFs decelerating as was the case for EIT waves (Warmuth & Mann 2011). However, in the full speed range, acceleration is distributed more or less around zero. This is partly because we fit the distance vs time only until the propagation is clearly altered by active regions or coronal holes. Furthermore, there seems no difference in the speed vs acceleration pattern when the LCPF is associated or not associated with a type II burst. Figure 6 shows the distribution of linear speed with respect to the flare class, CME level (see the previous section), association with type II bursts and appearance of the front at 171 Å. On average the speed appears to be correlated with these observables. Higher speeds are seen in intense flares and energetic CMEs, and when type II bursts are associated and the 171 Å front appears in intensity enhancement. This is summarized in the average and median speeds for each of the observables. However, the distribution is broad and it is possible to find high-speed LCPFs without the above properties.

Lastly, we compare the speeds of LCPFs and CMEs (or outflows) observed by COR-1 in the heliocentric distance range of $(1.5-4)R_{\odot}$, for a subset of 86 events for which the source region is located limbward of 60° longitude from either or both STEREO spacecraft. The speeds measured in this view may be closer to the true CME speeds because they are less susceptible to projection and visibility effects (e.g., Burkepile et al. 2004; Yashiro et al. 2005). Figure 7(b) gives an example of the distance-time or height-time plot of a CME along the cut as shown in Figure 7(a). We make sure that the cut passes both the LCPF as projected on the limb and the dominant direction of CME propagation. In Figure 8 we compare the speeds of 86 LCPFs and associated CMEs (or outflows) as observed by COR-1 as limb events. We assume the uncertainty of 25 Mm in locating the CME front (Figure 7(b)). The two speeds do not seem to be strongly correlated, irrespective of whether the LCPF is associated with a type II burst.

5. Discussion

We have found 171 LCPFs during April 2010–January 2013 by manually inspecting AIA images, and made an online catalog of LCPFs. This is not meant to be a complete catalog, but we believe that most “major” LCPFs have been included. Some minor events discussed by Zheng et al. (2011, 2012c, 2012d, 2013) are not included in Table 1 because of our working definition of LCPF that it should be $>45^{\circ}$ wide and be observed more than 200 Mm away from the eruption center. The last column in Table 1 shows the references so far published to discuss the individual LCPFs either directly or indirectly. To date a small number of relatively old events have been studied.

As captured in the movies included in the catalog, LCPFs have widely different appearances, many of which are not circular, as was thought to be “typical” for EIT waves (see a review by Wills-Davey & Attrill 2009). Some LCPFs appear predominantly over the limb as seen in AIA images. Here we do not discuss them because the speeds obtained by EUVI in disk view are sometimes far from those measured by AIA along the limb, although such limb events have been used in the context of the numerical simulations that have helped us recognize the coexistence of wave and CME-related components (Downs et al. 2011, 2012). Some events close to the limb may even show more radial motions than lateral, marginally producing LCPFs (e.g., 2010 August 1 event, see Schrijver et al. 2011; Liu et al. 2011). It is to be seen how these “untypical” events will be included in the automatic detection software being developed. Such software should make it easier to conduct ensemble studies of LCPFs on more involved parameters. This study may help validate the software.

It is widely accepted that EIT waves are more intimately associated with CMEs than

with flares (Biesecker et al. 2002; Cliver et al. 2005; Chen 2006). In many LCPFs, however, the associated CMEs are quite insignificant, suggesting that the processes close to the Sun that allow fast lateral expansion seems to be a key for certain LCPFs (Patsourakos & Vourlidas 2012). However, it is not clear whether such processes accompany all CMEs and the height of their occurrences possibly determines LCPF detection. They are certainly not part of flare processes, since for many LCPFs the associated flares are less intense than the GOES C-class. It is thus important to understand how the lateral expansion starts. The present study primarily deals with the global properties in 4×4 rebinned full-disk images, with the pixel resolution comparable to that of EIT. On that scale, we can easily miss out important changes within active regions that may directly indicate lateral expansions. Unlike EIT, however, we can go back to the full resolution zooming into the active region and immediate neighborhood, where, in combination with vector magnetic field data from the *Helioseismic and Magnetic Imager* (HMI; Scherrer et al. 2012), we may be able to observe the first signatures of the lateral expansion. In other words, this information may help us understand the range of variations in how solar eruptions occur.

Even though there were criticisms (e.g., Attrill 2010) to the idea of deflection of EIT waves at coronal holes (e.g., Gopalswamy et al. 2009), AIA data show that such deflections or alterations of the front are quite common at non-quiet-Sun magnetic field elements. Movies included in our online catalog of LCPFs as described in §2 immediately show us how LCPFs propagate outside quiet-Sun regions. It is likely that these deflections and subsequent propagations indicate that they are fast-mode MHD waves, which at greater distances likely represent freely propagating waves. In this work the speeds of LCPFs are measured before they encounter active regions or coronal holes and get deflected. It is in this early stage that LCPFs are poorly understood. Models indicate that in the early development of LCPFs the waves are not easily separable from CME loops (Downs et al. 2012). Observationally, we may see both components (Patsourakos & Vourlidas 2012). Further progress requires more detailed analysis of the kinematics (including the amplitude and width of the front, e.g., Veronig et al. 2010) and thermodynamic properties, and runs of MHD simulations in wider parameter space than what have been done for relatively modest eruptions (Cohen et al. 2009; Downs et al. 2011, 2012).

As in Figure 5, we fail to confirm distinct kinematic properties as found by Warmuth & Mann (2011) in EIT and EUVI data that may indicate their different origins. This is partly because our measurements are restricted to the early stages of LCPFs. In other words, in at least a number of cases, the apparent deceleration of EIT waves probably resulted from deflection by coronal holes or active regions at large distances. In the past, several examples of deceleration were found by comparing the trajectories of EIT waves with those of faster waves observed in other wavelengths such as $H\alpha$, soft X-rays, He I λ 10830, and radio. It is possible

that EIT waves observed in other wavelengths represent a subset of “strong” events, and that AIA has observed only a few of them. Indeed, we know of only two Moreton-Ramsey waves since SDO launch (Asai et al. 2012, White, 2012, personal communication), but it is possible that we may find more with more extensive search. Now waves in other wavelengths can be directly compared with LCPFs without extrapolation in time. Such comparisons will be useful for further clarifying the relation between the wave and CME components in LCPFs in the early phase and probing the origin of large-amplitude fast MHD waves. The sharpness of the front may also be useful for answering these questions, since in the past “sharp” waves accompanied EIT waves observed in multiple wavelengths (Thompson et al. 2000b). The association of LCPFs with Moreton-Ramsey waves and type II bursts may also depend on the angle of the propagating front with respect to the solar surface that can affect the downward pressure and the shock geometry important for particle acceleration (Liu et al. 2012).

We find in Figure 6 some correlation between the speeds of LCPFs and indicators for the magnitude of eruption or energy release. However the correlation is not strong. There is an expectation that the correlation could be made tighter if the magnitude of energy release were more properly formulated such as using the X-ray fluence rather than the peak flux—which may not be trivial especially for small flares—, but it is more likely that the occurrence and speed of LCPFs depend on the external conditions rather than the energy release mechanism. This is consistent with the fact that a small number of active regions are very prolific in LCPFs (see Table 1).

In this study we do not deal with LCPFs at greater distances beyond surrounding active regions and coronal holes. It appears that such LCPFs may be freely propagating MHD waves. They may still play an important role in acceleration and transport of solar energetic particles (e.g., Krucker et al. 1999; Rouillard et al. 2012) and in sympathetic flares and eruptions (e.g., Schrijver et al. 2013). For these questions, we need to analyze data in longer time ranges beyond individual LCPFs, and the 360° view of the Sun made by combining AIA and EUVI data (Olmedo et al. 2012) would be extremely useful.

Many papers have posed questions like “What is the nature of EIT waves?” as if a single scheme could explain the phenomena in a unified way even though different examples appear to have widely different properties. It is more productive to characterize individual LCPFs to understand when, where and how both wave and CME components appear (Schrijver et al. 2011; Downs et al. 2012). This study may help to put into perspective the individual LCPFs that will be studied in detail.

This work was supported by the AIA contract NNG04EA00C to LMSAL. WL acknow-

ledges NASA grant NNX11AO68G. We thank the referee for useful suggestions for us to improve the manuscript.

REFERENCES

- Asai, A., Ishii, T. T., Kitai, R., Ichimoto, K., UsNo, S., Nagata, S., Morita, S., Nishida, K., Shiota, D., Oi, A., Akioka, M., & Shibata, K. 2011, *ApJ*, 745, L18
- Attrill, G. D. R. 2010, *ApJ*, 718, 494
- Attrill, G. D. R., Harra, L. K., van Driel-Gesztelyi, L., & Démoulin, P. 2007, *ApJ*, 656, L101
- Biesecker, D. A., Myers, D. C., Thompson, B. J., Hammer, D. M., & Vourlidas, A. 2002, *ApJ*, 569, 1009
- Burkepile, J. T., Hundhausen, A. J., Stanger, A. L., St. Cyr, O. C., & Seiden, J. A. 2004, *J. Geophys. Res.*, 109, A03103
- Chen, P. F. 2006, *ApJ*, 641, L153
- Chen, P. F., & Wu, Y. 2011, *ApJ*, 732, L20
- Chen, P. F., Wu, S. T., Shibata, K., & Fang, C. 2002, *ApJ*, 572, L99
- Chen, F., Ding, M. D., Chen, P. F., & Harra, L. K. 2011, *ApJ*, 740, 116
- Cheng, X., Zhang, J., Olmedo, O., Vourlidas, A., Ding, M. D., & Liu, Y. *ApJ*, 745, L5
- Cliwer, E. W., Laurenza, M., Storini, M., & Thompson, B. J. 2005, *ApJ*, 631, 604
- Cohen, O., Attrill, G. D. R., Manchester, W. B., IV & Wills-Davey, M. J. 2009, *ApJ*, 705, 587
- Dai, Y., Ding, M. D., Chen, P. F., & Zhang, J. 2012, *ApJ*, 759, 55
- Delaboudinière, J.-P. et al. 1995, *Sol. Phys.*, 162, 291
- Delannée, C. & Aulanier, G., *Sol. Phys.*, 190, 107
- Downs, C., Rouseff, I., van der Holst, B., Lugaz, N., Sokolov, I., & Gombosi, T.I. 2011, *ApJ*, 728, 2
- Downs, C., Rouseff, I., van der Holst, B., Lugaz, N., & Sokolov, I. 2012, *ApJ*, 750, 134

- Gopalswamy, N., Yashiro, S., Temmer, M., Davilla, J., Thompson, W. T., Jones, S., McAteer, R. T. J., Wuelser, J.-P., Freeland, S., & Howard, R. A. 2009, *ApJ*, 691, L123
- Gopalswamy, N., Nitta, N., Akiyama, S., Mäkelä, P., & Yashiro, S. 2012, *ApJ*, 744, 72
- Gopalswamy, N. et al. *Adv. Space Res.*, 51, 1981
- Gosain, S., & Foullon, C. 2012, *ApJ*, 761, 103
- Howard, R. A. et al. 2008, *Space Sci. Rev.*, 136, 67
- Harra, L. K., Sterling, A. C., Gömöry, P., & Veronig, A. 2011, *ApJ*, 737, L4
- Hurlburt, N. et al. 2012, *Sol. Phys.*, 275, 67
- Kienreich, I. W., Temmer, M., & Veronig, A. M. 2011, *ApJ*, 703, L118
- Kozarev, K. A., Korreck, K. E., Lobzin, V. V., Weber, M. A., & Schwadron, N. A. 2011, *ApJ*, 733, L25
- Krucker, S., Larson, D. E., Lin, R. P., & Thompson, B. J. 1999, *ApJ*, 519, 864
- Kumar, P., & Manoharan, P. K., 2013, *A&A*, 553, A109
- Kumar, P., Cho, K.-S., Chen, P. F., Bong, S.-C., Park, S.-H., & Kim, Y. H. 2013, *Sol. Phys.*, 282, 523
- Lemen, J. R. et al. 2012, *Sol. Phys.*, 275, 17
- Li, T., Zhang, J., Yang, S., & Liu, W., 2012, *ApJ*, 746, 13
- Liu, W., Nitta, N. V., Schrijver, C. J., Title, A. M., & Tarbell, T. D. 2010, *ApJ*, 723, L53
- Liu, W., Title, A. M., Zhao, J., Ofman, L., Schrijver, C. J., Aschwanden, M. J., De Pontieu, B., & Tarbell, T. D. 2011, *ApJ*, 736, L13
- Liu, W., Ofman, L., Nitta, N. V., Aschwanden, M. K., Schrijver, C. J., Title, A. M. & Tarbell, T. D. 2012, *ApJ*, 753, 52
- Long, D. M., Gallagher, P. T., McAteer, R. T. J., & Bloomfield, D. S. 2008, *ApJ*, 680, L81
- Long, D. M., Gallagher, P. T., McAteer, R. T. J., & Bloomfield, D. S. 2011a, *A&A*, 531, A42
- Long, D. M., DeLuca, E. E., & Gallagher, P. T. 2011b, *ApJ*, 741, L23

- Ma, S., Raymond, J. C., Golub, L., Lin, J., Chen, H., Grigis, P., Testa, P., & Long, D. 2011, *ApJ*, 738, 160
- Markwardt, C. B. 2009, in *ASP Conf. Ser. 411, Astronomical Data Analysis Software and Systems XVIII*, ed. D. A. Bohlander, D. Durand, & P. Dowler (San Francisco, CA: ASP), 251
- Martens, P. C. H. et al. 2012, *Sol. Phys.*, 275, 79
- Moreton, G. E., & Ramsey, H. E. 1960, *PASP*, 72, 357
- Moses, D. et al. 1997, *Sol. Phys.*, 175, 571
- Nitta, N. V., Aschwanden, M. J., Freeland, S. L., Lemen, J. R., Wuelser, J.-P., & Zarro, D. M. 2013, *Sol. Phys.*, Submitted
- Ofman, L., & Thompson, B. J. 2002, *ApJ*, 574, 440
- Olmedo, O., Vourlidas, A., Zhang, J., & Cheng, X. 2012, *ApJ*, 756, 143
- Patsourakos, S., & Vourlidas, A. 2009, *ApJ*, 700, L182
- Patsourakos, S., Vourlidas, A., Wang, Y.-M., Stenborg, G., & Thernisien, A. 2009, *Sol. Phys.*, 259, 49
- Patsourakos, S., Vourlidas, A., & Stenborg, G. 2010, *ApJ*, 724, L188
- Patsourakos, S. & Vourlidas, A. 2012, *Sol. Phys.*, 281, 187
- Podladchikova, O., & Berghmans, D. 2005, *Sol. Phys.*, 228, 265
- Rouillard, A. P., Sheeley, N. R., Jr., Tulka, A., Vourlidas, A., Ng, C. K., Rakowski, C. R., Cohen C. M. S., Mewaldt, R. A., Mason, G. M., Reames, D., Savani, N. P., St. Cyr, O. C., & Szabo, A. 2012, *ApJ*, 752, 44
- Scherrer, P. H. et al. 2012, *Sol. Phys.*, 275, 207
- Schmidt, J. M., & Ofman, L. 2010, *ApJ*, 713, 1008
- Schrijver, C. J., Aulanier, G., Title, A. M., Pariat, E., & Delannée, C. 2011, *ApJ*, 738, 167
- Schrijver, C. J., Title, A. M., Yeates, A. R. & DeRosa, M. L. 2013, *ApJS*, in press
- Shen, Y., & Liu, Y. 2012a, *ApJ*, 752, L23

- Shen, Y., & Liu, Y. 2012b, *ApJ*, 753, 53
- Shen, Y., & Liu, Y. 2012c, *ApJ*, 754, 7
- Thompson, B. J., Plunkett, S. P., Gurman, J. B., Newmark, J. S., St. Cyr, O. C., Michels, D. J., & Delaboudinière, J.-P. 1998, *Geophys. Res. Lett.*, 14, 2461
- Thompson, B. J., Gurman, J. B., Neupert, W. M., Newmark, J. S., Delaboudinière, J.-P., St. Cyr, O. C., Stezelberger, S., Dere, K. P., Howard, R. A., & Michels, D. J., 1999, *ApJ*, 517, L151
- Thompson, B. J., Cliver, E. W., Nitta, N., Delannée, C., & Delaboudinière, J.-P. 2000a, *Geophys. Res. Lett.*, 27, 1431
- Thompson, B. J., Reynolds, B., Aurass, H., Gopalswamy, N., Gurman, J. B., Hudson, H. S., Martin, S. F., & St. Cyr, O. C. 2000b, *Sol. Phys.*, 193, 161
- Thompson, B. J., & Myers, D. C. 2009, *ApJS*, 183, 225
- Uchida, Y. 1968, *Sol. Phys.*, 4, 30
- Veronig, A. M., Muhr, N., Kienreich, I. W., Temmer, M., & Vršnak, B. 2010, *ApJ*, 716, L57
- Veronig, A. M., Gömöry, P., Kienreich, I. W., Muhr, N., Vršnak, B., Temmer, M., & Warren, H. P. 2011, *ApJ*, 743, L10
- Vršnak, B., Warmuth, A., Temmer, M., Veronig, A., Magdalenic, J., & Karlický, M. 2006, *A&A*, 448, 739
- Wang, Y.-M. 2000, *ApJ*, 543, L89
- Wang, H., Shen, C., & Lin, J. 2009, *ApJ*, 700, 1716
- Warmuth, A., & Mann, G. 2011, *A&A*, 532, A151
- Warmuth, A., Vršnak, B., Aurass, H., & Hanslmeier, A. 2001, *ApJ*, 560, L105
- Warmuth, A., Vršnak, B., Magdalenic, J., Hanslmeier, A., & Otruba, W. 2004, *A&A*, 418, 1101
- Wills-Davey, M. J., & Thompson, B. J. 1999, *Sol. Phys.*, 190, 467
- Wills-Davey, M. J., & Attrill, G. D. R. 2009, *Space Sci. Rev.*, 149, 325
- Wills-Davey, M. J., DeForest, C. E., & Stenflo, J. O. 2007, *ApJ*, 664, 556

- Wu, S. T., Zheng, H., Wang, S., Thompson, B. J., Plunkett, S. P., Zhao, X. P., & Dryer, M. 2001, *J. Geophys. Res.*, 106, 25089
- Wu, S. T., Li, B., Wang, S., & Zheng, H. 2005, *J. Geophys. Res.*, 110, A11102
- Wuelser et al. 2004, *Proc. SPIE*, 5171, 111
- Yashiro, S., Gopalswamy, N., Akiyama, S., Michalek, G., & Howard, R.A. 2005, *J. Geophys. Res.*, 110, A12S05
- Zheng, R., Jiang, Y., Hong, J., Yang, J., & Yang, B. 2011, *ApJ*, 739, L39
- Zheng, R., Jiang, Y., Yang, J., Bi, Y., Hong, J., Yang, B., & Yang, D. 2012a, *ApJ*, 747, 67
- Zheng, R., Jiang, Y., Yang, J., Bi, Y., Hong, J., Yang, D., & Yang, B. 2012b, *ApJ*, 753, 112
- Zheng, R., Jiang, Y., Yang, J., Bi, Y., Hong, J., Yang, D., & Yang, B. 2012c, *ApJ*, 753, L29
- Zheng, R., Jiang, Y., Yang, J., Bi, Y., Hong, J., Yang, B., & Yang, D. 2012d, *A&A*, 541, A49
- Zheng, R., Jiang, Y., Yang, J., Bi, Y., Hong, J., Yang, B., & Yang, D. 2013, *ApJ*, 764, 70
- Zhukov, A. N., & Auchère, F. 2004, *A&A*, 427, 705

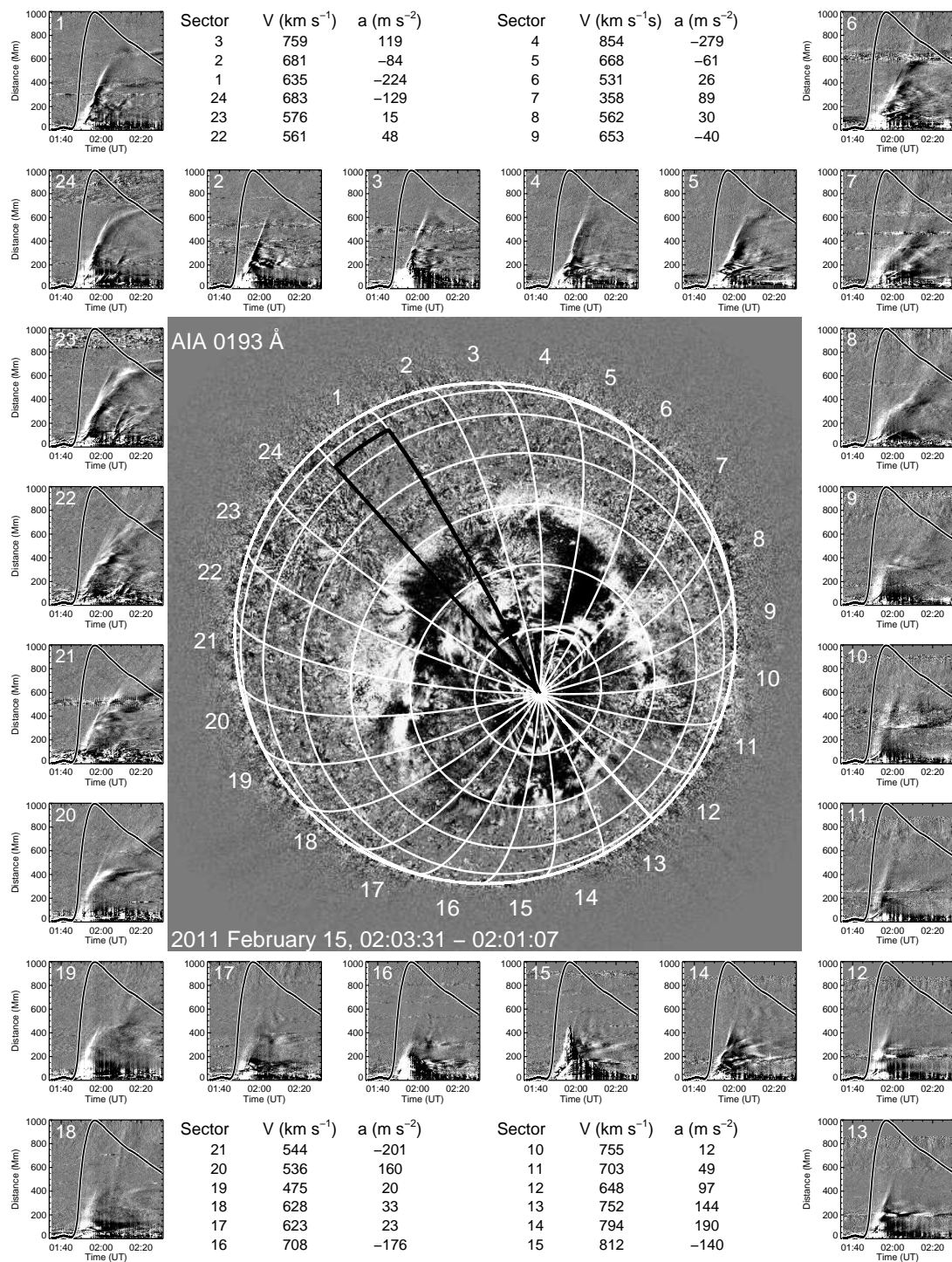


Fig. 1.— This figure shows 24 running-difference distance-time plots made from AIA images in 193 Å channel for the 2011 February 15 LCPCF. The plots are made in equally spaced sectors that are bounded by two great circles passing through the flare, as indicated in the image placed in the center. The normalized GOES 1–8 Å light curve is added to each distance-time plot. The distance is measured along the great circle. The distance of 1000 Mm is encircled in black in sector 1. The measured linear speed and constant acceleration are also shown.

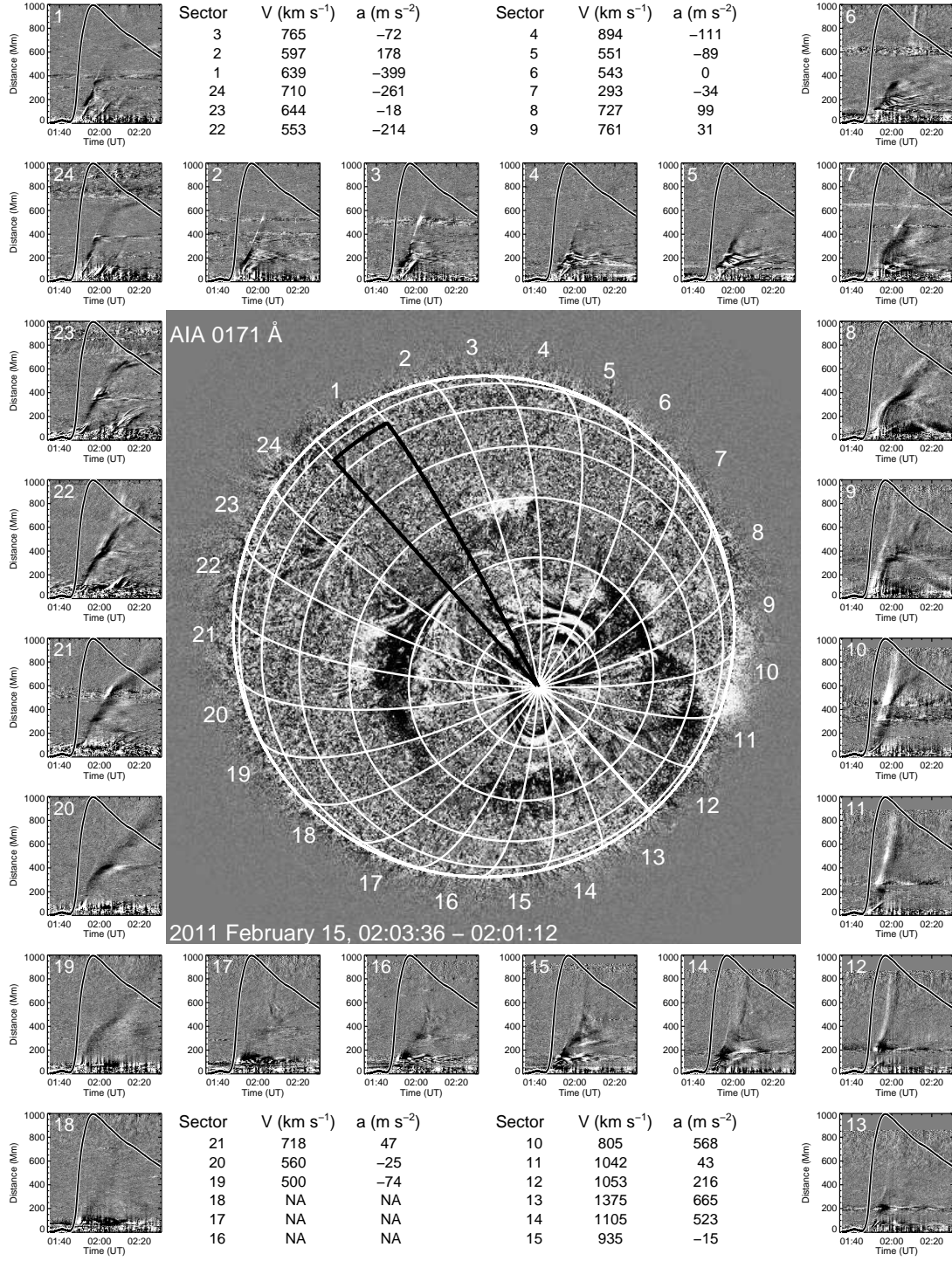


Fig. 2.— Same as Figure 1 but in 171 Å.

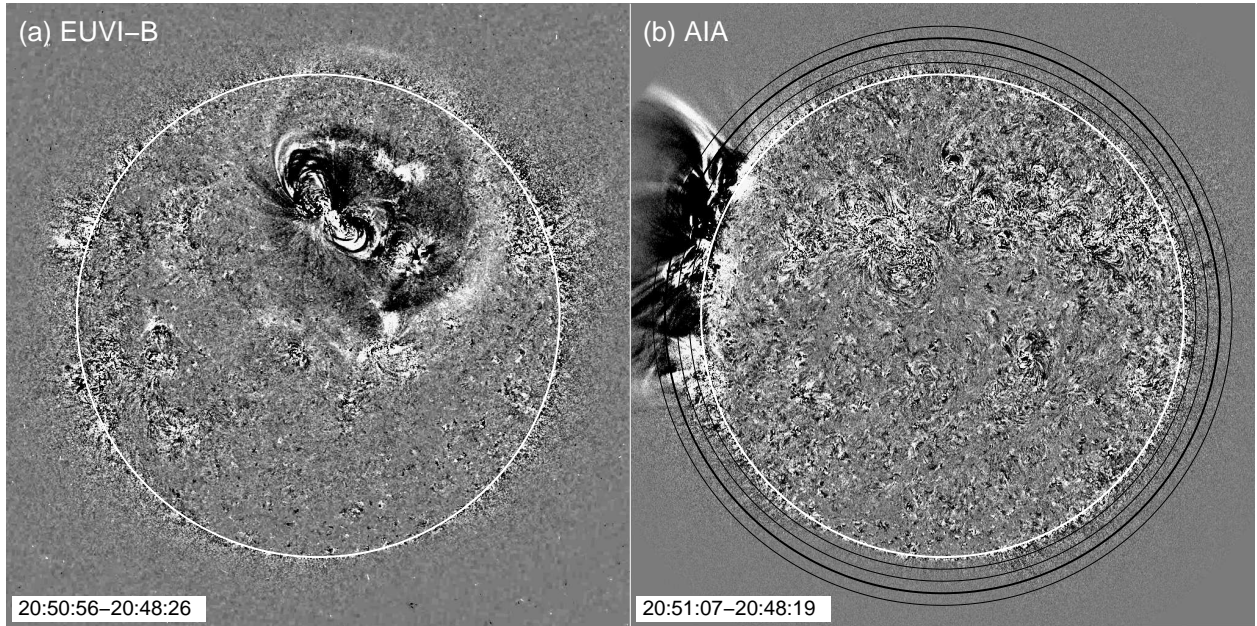


Fig. 3.— An example of LCPF seen predominantly along the limb with little presence on disk as seen by AIA. Panel (b) shows an AIA 193 Å difference image with black circles of heliocentric distances of $1.05R_{\odot}$, $1.10R_{\odot}$, $1.15R_{\odot}$ and $1.20R_{\odot}$ in addition to the limb in white. The circle of $1.15R_{\odot}$ is shown in a thick line. The same front is seen by EUVI on STEREO-B as a disk event as shown in panel (a).

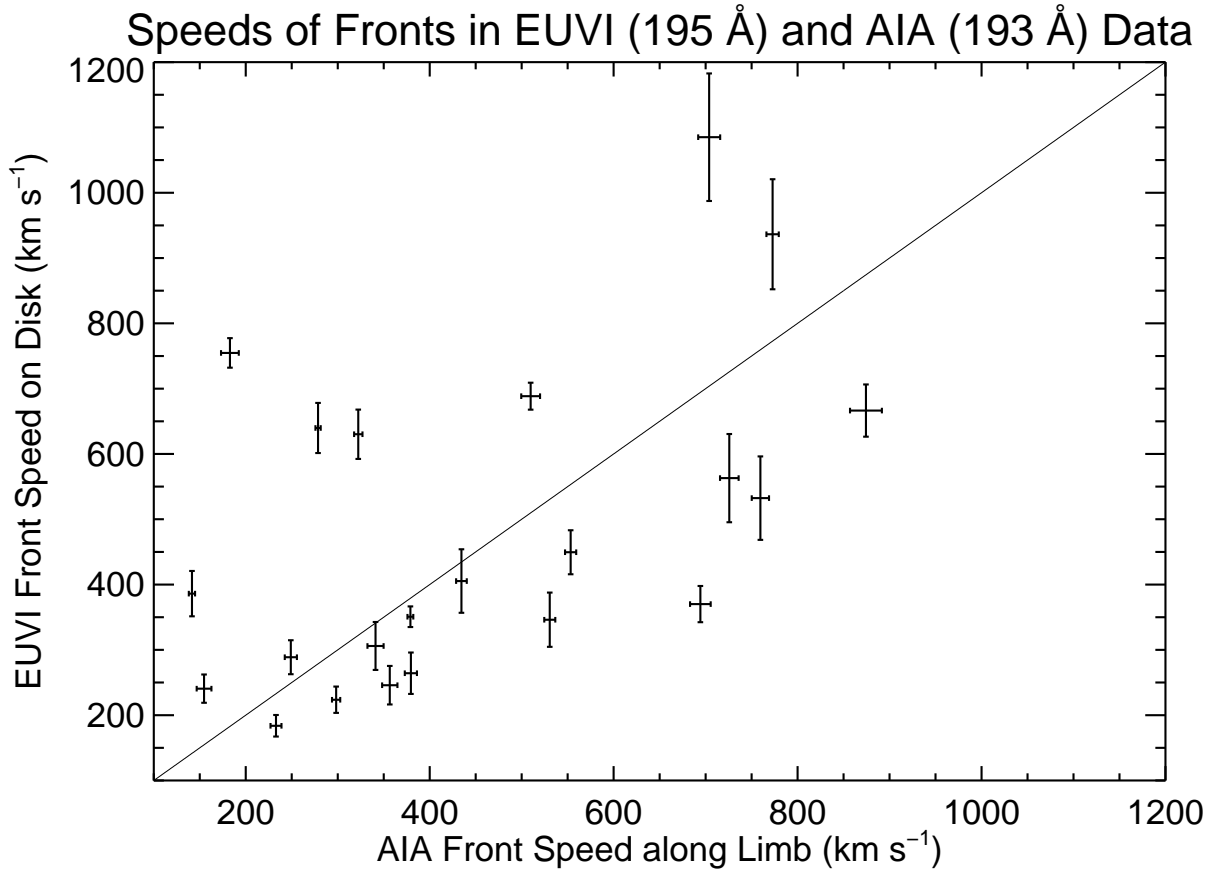


Fig. 4.— Comparison of the speeds of the same fronts measured along the limb (at the heliocentric distance of $1.15 R_{\odot}$) by AIA and along great circles on disk by EUVI. The line gives $v_{\text{AIA}} = v_{\text{EUVI}}$ as a visual guide.

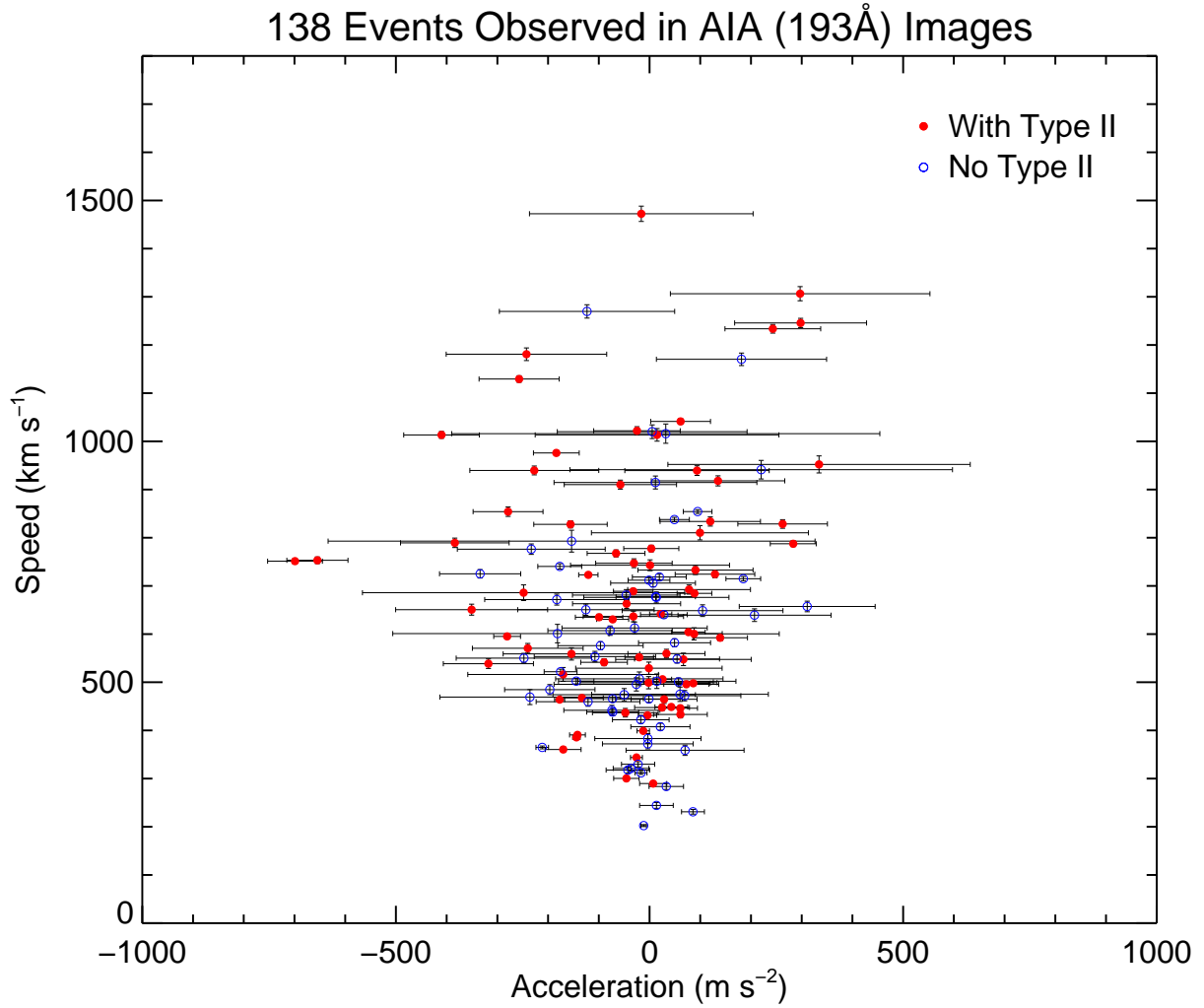


Fig. 5.— Linear speed of the propagating front in 193 Å plotted against constant acceleration in 138 events that allow us to trace the front on disk. Data are plotted separately for events with and without an associated type II radio burst.

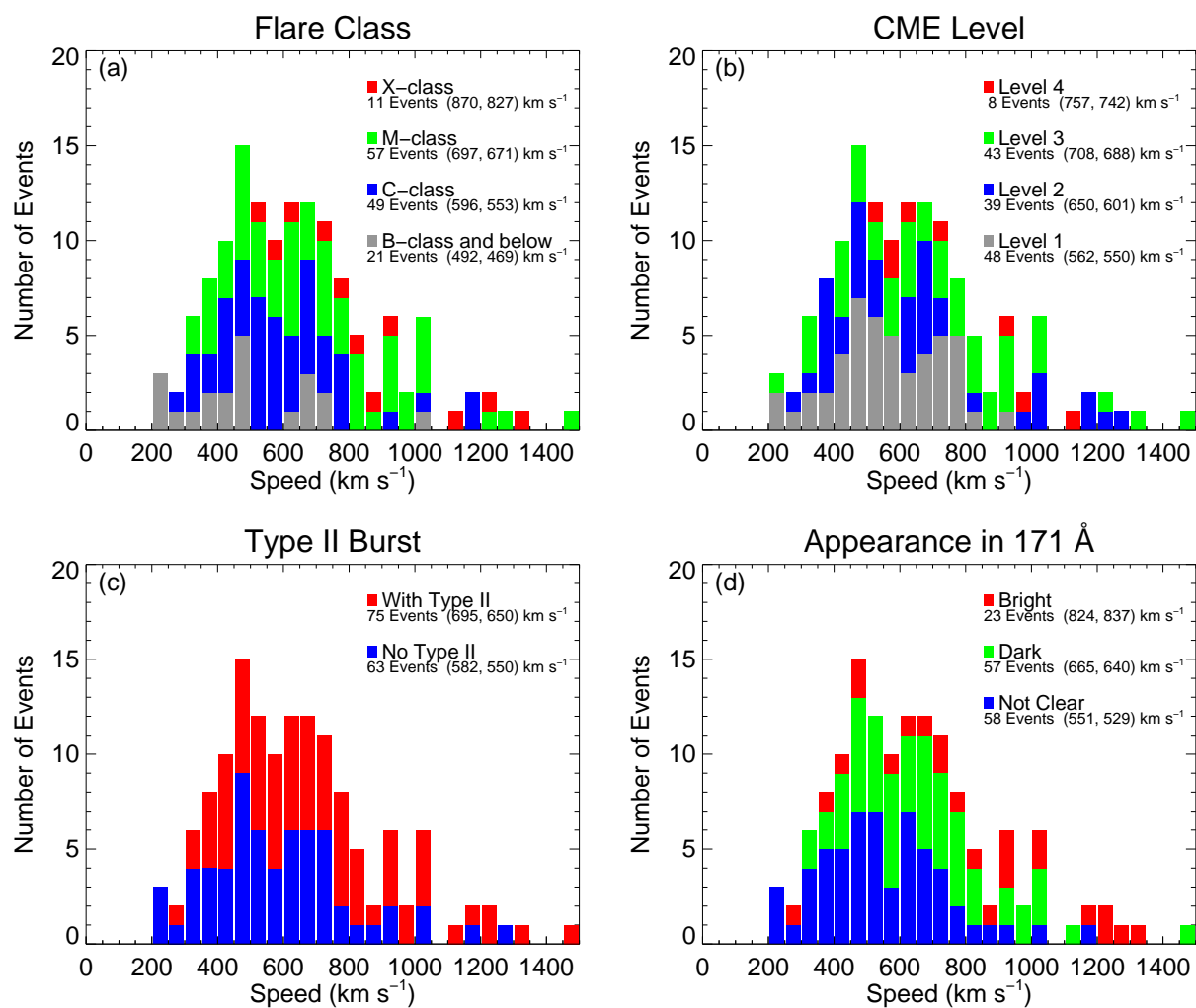


Fig. 6.— Histogram of the speed of LCPFs plotted for four observables. Average and median speeds are shown for each category of the observables.

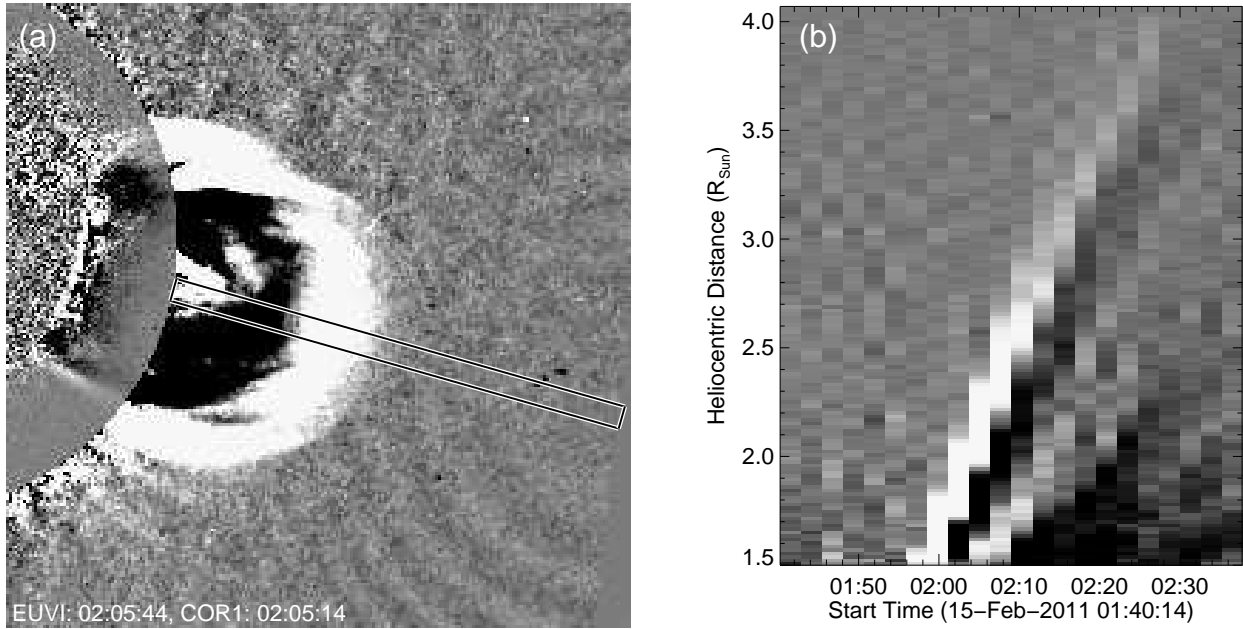


Fig. 7.— (a) Composite of EUVI and COR-1 difference images. The distance-time plot of COR-1 data is shown in (b) for the cut indicated by a rectangle in (a).

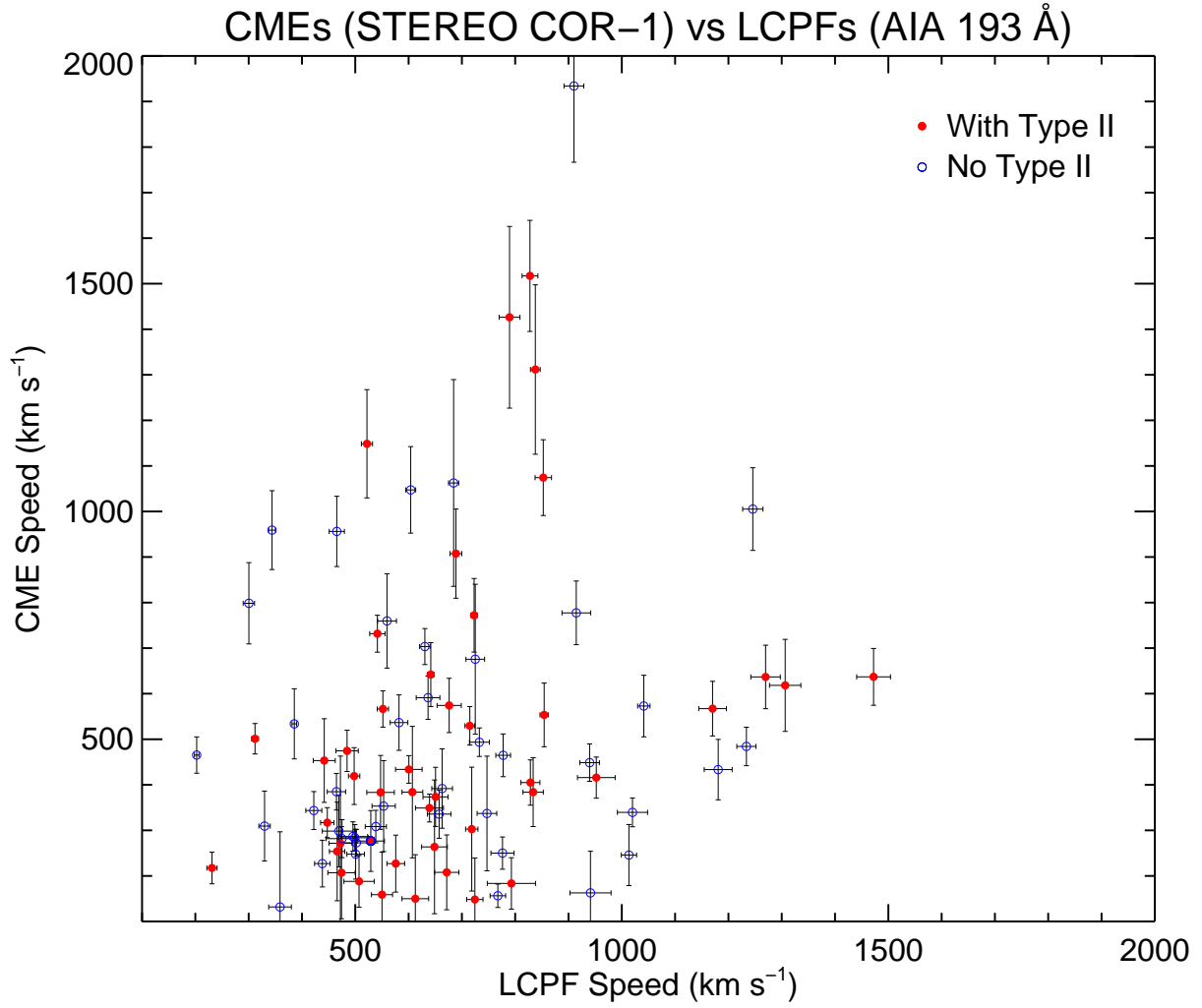


Fig. 8.— The CME speed as derived from COR-1 data plotted against the speed of LCPFs for events observed limbward of the longitude of 60° by STEREO.

Table 1. The 171 LCPFs

Date	Flare				LCPF			Others				References ^b
	Start Time	GOES Class	Location	AR	Speed (km s ⁻¹)	Direction	171 Å ^a	CME Level	Type II Burst	STEREO Limb		
2010 Apr 8	02:30	B3.7	N24 E17	11060	203	S	N	3	N	A	15	
2010 May 4	06:30	B1.3	S26 E04	11066	469	E	N	2	N	BA	...	
2010 May 8	20:04	C2.4	N40 W75	11069	502	S	D	2	N	
2010 Jun 12	00:53	M2.0	N23 W43	11081	386	SE	D	2	Y	B	3, 11	
2010 Jun 12	09:04	C6.1	N22 W52	11081	391	SE	N	2	Y	
2010 Jun 13	05:30	M1.0	S25 W84	11079	360	NE	D	2	Y	...	6, 7, 11, 19, 21	
2010 Jul 16	15:08	A8	S21 W20	N-AR	231	NW	N	1	N	B	...	
2010 Jul 27	08:46	A6	S17 W48	N-AR	474	N	B	1	N	B	2	
2010 Aug 1	07:22	C3.1	N20 E36	11092	312	N	D	3	N	A	16	
2010 Aug 7	17:55	M1.0	N11 E34	11093	631	S	B	3	Y	A	...	
2010 Aug 14	09:38	C4.4	N14 W54	11093	431	S	D	3	Y	...	18	
2010 Aug 18	04:45	C4.5	N14 W105	11093	Limb	
2010 Sep 8	23:05	C3.3	N20 W90	11105	Limb	9, 17	
2010 Oct 16	19:07	M2.9	S20 W26	11112	1013	NW	D	2	Y	B	13	
2010 Nov 03	05:54	C3.8	S20 E98	11121	
2010 Nov 03	12:43	C3.4	S20 E97	11121	
2010 Nov 11	18:52	B9.4	N12 E28	11124	359	S	N	1	N	A	27	
2010 Nov 11	19:40	C1.3	N13 E27	11124	466	SE	D	1	N	A	27	
2010 Nov 11	20:47	B9.0	N13 E26	11124	472	SE	D	1	N	A	27	
2010 Nov 15	14:36	B7.6	S22 W44	11123	365	NE	N	2	N	
2010 Dec 15	14:31	B2.2	N20 W55	11134	651	E	N	2	Y	
2010 Dec 31	04:18	C1.3	N13 W57	11138	446	NE	D	2	Y	
2011 Jan 27	08:40	B6.6	N13 W82	11149	
2011 Jan 27	11:53	C1.2	N13 W85	11149	399	SE	B	2	Y	...	5	
2011 Jan 28	00:44	M1.3	N13 W90	11149	464	E	D	3	Y	
2011 Feb 11	21:31	B8.1	N11 E105	11161	Limb	
2011 Feb 13	17:28	M6.6	S20 E04	11158	498	E	B	2	Y	BA	8	
2011 Feb 14	02:35	C1.6	S21 E04	11158	501	N	D	1	N	BA	...	
2011 Feb 14	04:29	C8.3	S20 W01	11158	501	N	N	1	N	BA	...	
2011 Feb 14	06:51	C6.6	S20 W01	11158	657	NE	D	1	N	BA	...	
2011 Feb 14	12:41	C9.4	S20 W02	11158	663	NE	D	2	Y	BA	8	
2011 Feb 14	17:20	M2.2	S20 W05	11158	829	NE	D	2	Y	BA	...	
2011 Feb 14	19:23	C6.6	S20 W05	11158	639	NE	D	1	N	BA	...	
2011 Feb 15	00:31	C2.7	S20 W07	11158	651	NE	D	1	N	BA	...	
2011 Feb 15	01:44	X2.2	S20 W12	11158	854	N	D	3	Y	BA	20, 22	
2011 Feb 15	03:05	<C1	S21 W08	11158	613	NE	N	1	N	BA	...	
2011 Feb 15	04:27	C4.8	S21 W09	11158	582	NE	D	1	N	BA	...	
2011 Feb 15	05:07	B1.3	N22 E47	11161	284	S	B	1	N	
2011 Feb 15	07:11	B2.7	N21 E46	11161	318	S	D	1	N	
2011 Feb 15	14:32	C4.8	S20 W16	11158	555	N	D	1	N	BA	...	
2011 Feb 16	14:19	M1.6	S22 W30	11158	496	N	N	1	Y	...	10, 26	
2011 Feb 17	21:30	C1.1	S18 W45	11158	571	N	B	1	Y	
2011 Feb 24	07:23	M3.5	N16 E88	11163	433	W	D	3	Y	

Table 1—Continued

Date	Flare				LCPF			Others				References ^b
	Start Time	GOES Class	Location	AR	Speed (km s ⁻¹)	Direction	171 Å ^a	CME Level	Type II Burst	STEREO Limb		
2011 Mar 7	13:45	M1.9	N12 E21	11166	300	N	N	3	Y	BA	8	
2011 Mar 7	19:43	M3.7	N30 W47	11164	506	S	D	4	Y	
2011 Mar 8	03:37	M1.5	S21 E72	11171	449	NW	B	3	Y	
2011 Mar 8	18:50	<B1	N10 W01	11166	442	W	D	1	N	BA	...	
2011 Mar 8	19:46	M1.4	S19 W90	11165	Limb	
2011 Mar 12	04:33	M1.3	N05 W36	11166	753	S	D	1	Y	
2011 Mar 12	15:19	C9.6	N05 W39	11166	751	S	N	1	Y	
2011 Mar 24	12:01	M1.0	S15 E44	11176	712	NW	D	1	N	
2011 Mar 25	23:08	M1.0	S12 E26	11176	834	NW	D	1	Y	B	12	
2011 Mar 27	05:00	A8	N17 E101	N-AR	Limb	
2011 May 9	20:42	C5.4	N20 E91	N-AR	Limb	
2011 May 11	02:23	B8.1	N18 W52	N-AR	467	SE	D	3	Y	
2011 May 15	23:25	C4.8	N11 W47	11208	706	S	N	2	N	
2011 May 29	10:08	M1.4	S22 E65	11226	810	NW	N	3	Y	
2011 May 29	20:11	C8.7	S18 E68	11227	Limb	
2011 May 30	10:48	C2.8	S18 E60	11227	290	NW	N	2	Y	...	23	
2011 Jun 1	02:37	C2.6	S18 E37	11228	548	NW	D	1	N	
2011 Jun 1	16:50	C2.9	S19 E19	11226	408	NW	D	1	N	
2011 Jun 2	07:38	C1.4	S19 E20	11227	465	NW	D	3	N	B	...	
2011 Jun 7	06:16	M2.5	S21 W54	11226	976	E	D	4	Y	...	4, 14	
2011 Jul 3	00:01	B9.5	N14 W24	11244	685	S	D	2	Y	BA	...	
2011 Jul 11	10:37	C2.6	S17 E06	11249	601	SW	N	2	Y	BA	...	
2011 Jul 30	02:06	M9.3	N15 E35	11261	383	S	N	1	N	
2011 Aug 2	06:00	M1.4	N15 W14	11261	560	S	D	3	Y	BA	...	
2011 Aug 3	13:17	M6.0	N17 W30	11261	604	S	D	3	Y	A	...	
2011 Aug 4	03:41	M9.3	N17 W37	11261	910	S	B	4	Y	A	...	
2011 Aug 8	18:00	M3.5	N16 W63	11263	559	SE	D	4	Y	
2011 Aug 9	07:48	X6.9	N16 W72	11263	743	SE	D	4	Y	...	1, 24	
2011 Aug 10	15:46	A1	N20 E55	N-AR	686	S	N	2	Y	
2011 Aug 11	09:34	C6.2	N16 W102	11263	Limb	
2011 Sep 4	04:36	C9.0	S20 W108	11284	Limb	
2011 Sep 6	01:35	M5.3	N14 W07	11283	1041	NW	B	3	Y	BA	...	
2011 Sep 6	22:12	X2.1	N14 W18	11283	1246	N	B	3	Y	BA	...	
2011 Sep 7	22:32	X1.8	N14 W28	11283	1307	N	B	3	Y	A	...	
2011 Sep 8	15:32	M6.7	N14 W40	11283	649	NE	N	1	N	A	...	
2011 Sep 9	06:01	M2.7	N16 W47	11283	
2011 Sep 22	10:29	X1.4	N12 E81	11302	595	W	D	4	Y	
2011 Sep 23	12:10	C3.2	N28 W52	11296	
2011 Sep 23	23:48	M1.9	N12 E65	11302	516	SW	N	2	Y	
2011 Sep 24	09:32	X1.9	N12 E62	11302	1129	SW	D	4	Y	...	25	
2011 Sep 24	12:33	M7.1	N15 E60	11302	640	SW	D	4	N	
2011 Sep 24	19:09	M3.0	N15 E60	11302	918	NW	B	3	Y	
2011 Sep 24	21:23	M1.2	S28 W65	11303	460	N	N	1	N	

Table 1—Continued

Flare					LCPF			Others			
Date	Start Time	GOES Class	Location	AR	Speed (km s ⁻¹)	Direction	171 Å ^a	CME Level	Type II Burst	STEREO Limb	References ^b
2011 Sep 24	23:45	M1.0	S28 W66	11303	601	NE	N	2	N
2011 Sep 25	02:27	M4.4	S28 W68	11303	372	N	N	2	N
2011 Sep 25	04:31	M7.4	N12 E50	11302	740	S	N	3	N
2011 Sep 25	09:25	M1.5	S28 W72	11303	321	N	N	1	N
2011 Sep 25	15:26	M3.7	N13 E43	11302	678	SW	D	2	N
2011 Sep 26	14:37	M2.6	N14 E30	11302	671	S	N	1	N	B	...
2011 Sep 27	20:34	C6.4	N14 E09	11302	550	S	N	1	N	BA	...
2011 Sep 29	12:07	C2.7	N10 W11	11302
2011 Sep 30	02:46	C1.0	N14 W32	11302	576	S	D	1	N	A	28
2011 Sep 30	03:47	C7.7	N10 E10	11305	793	S	N	1	N	BA	...
2011 Oct 1	09:44	M1.2	N10 W06	11305	733	S	N	3	Y	BA	...
2011 Oct 1	20:00	...	N24 E118
2011 Oct 2	00:37	M3.9	N10 W14	11305	715	S	D	3	N	BA	...
2011 Oct 2	21:41	C7.6	N10 W25	11305	607	S	D	2	N	BA	...
2011 Oct 3	02:34	C2.1	S13 W62	11302	Limb
2011 Oct 10	14:30	C4.5	S13 E03	11313	941	W	D	1	N	BA	...
2011 Oct 20	03:10	M1.6	N20 W95	11318	Limb
2011 Oct 21	12:53	M1.3	N06 W80	11319	592	E	N	3	Y
2011 Nov 9	13:04	M1.1	N20 E30	11342	642	NW	N	3	Y	B	...
2011 Nov 14	09:18	C5.2	N22 W63	11348	1014	E	N	2	Y
2011 Nov 15	00:07	<B1	N08 E30	11347	724	S	D	1	Y	B	...
2011 Nov 24	23:57	C1.5	S18 W20	11354	330	SE	N	2	N	A	...
2011 Nov 25	21:49	C2.4	N17 W62	11359	692	SE	N	1	Y
2011 Dec 13	03:08	B2.3	S17 E12	11374	719	W	D	1	N	BA	...
2011 Dec 22	01:56	C5.4	S19 W18	11381	448	N	N	2	Y	A	...
2011 Dec 25	08:49	C5.5	S21 W20	11387	776	E	D	1	N	A	...
2011 Dec 25	18:11	M4.0	S22 W26	11387	940	S	B	3	N	A	...
2011 Dec 25	20:23	C7.7	S21 W24	11387	725	E	D	2	N	A	...
2011 Dec 26	02:13	M1.5	S21 W33	11387	854	N	N	3	N	A	...
2011 Dec 26	11:16	C5.7	N18 W02	11384	676	NE	B	3	N	BA	...
2012 Jan 23	03:38	M8.7	N28 W21	11402	837	E	B	3	N	A	...
2012 Jan 27	17:37	X1.7	N27 W71	11402	635	E	N	3	Y
2012 Mar 2	17:29	M3.3	N18 E86	11429	Limb
2012 Mar 4	10:29	M2.0	N17 E64	11429	1016	SW	D	3	N
2012 Mar 5	03:25	X1.1	N17 E56	11429	915	SW	N	3	N	B	...
2012 Mar 7	00:02	X5.4	N18 E31	11429	828	W	N	3	Y	B	...
2012 Mar 7	01:05	X1.3	N18 E31	11429	789	W	N	3	Y	B	...
2012 Mar 9	03:22	M6.3	N17 E02	11429	689	W	D	3	Y	BA	...
2012 Mar 10	17:15	M8.4	N16 W24	11429	522	SE	N	3	N	A	...
2012 Mar 13	17:12	M7.9	N18 W61	11429	1022	E	B	3	Y
2012 Mar 14	15:08	M2.8	N14 E06	11432	485	S	N	2	N	BA	...
2012 Mar 17	20:32	M1.3	S20 W25	11434	548	NE	D	1	Y	A	...
2012 Mar 26	22:40	...	N18 E125	...	Limb

Table 1—Continued

Flare					LCPF			Others				References ^b
Date	Start Time	GOES Class	Location	AR	Speed (km s ⁻¹)	Direction	171 Å ^a	CME Level	Type II Burst	STEREO Limb		
2012 Apr 5	20:49	C1.5	N17 W32	11450	552	NE	N	3	Y	A	...	
2012 Apr 9	12:12	C3.9	N16 W63	11451	Limb	
2012 Apr 23	17:38	C2.0	N14 W17	11461	723	SE	B	1	Y	A	...	
2012 Apr 24	07:38	C3.7	N12 E80	11467	787	SW	D	3	Y	
2012 May 17	01:25	M5.1	N11 W76	11476	939	E	D	3	Y	
2012 Jun 3	17:48	M3.3	N17 E38	11496	1472	W	D	3	Y	B	...	
2012 Jun 6	19:54	M2.1	S18 W05	11494	1234	S	B	2	Y	A	...	
2012 Jun 23	07:02	C2.7	N17 W102	N-AR	Limb	
2012 Jul 2	10:43	M5.6	S18 E05	11515	1234	S	B	2	Y	B	...	
2012 Jul 2	19:59	M3.8	S17 E03	11515	1270	S	B	2	N	B	...	
2012 Jul 6	23:01	X1.1	S14 W59	11515	Limb	
2012 Jul 8	16:23	M6.9	S14 W85	11515	Limb	
2012 Jul 12	15:37	X1.4	S17 W02	11520	542	SW	N	3	Y	BA	...	
2012 Jul 31	10:46	C5.7	N18 E64	11535	
2012 Aug 13	12:33	C2.8	N23 W04	11543	1181	NW	N	2	Y	BA	...	
2012 Aug 14	00:23	C3.5	N23 W11	11543	1170	W	B	2	N	A	...	
2012 Aug 15	03:37	B8.5	N23 W25	11543	1020	N	D	2	N	A	...	
2012 Aug 16	12:41	C3.6	N23 W40	11543	
2012 Aug 17	22:23	B5.9	N23 W62	11543	
2012 Aug 31	19:45	C8.4	S27 E47	11562	
2012 Sep 15	22:23	B9.6	N26 W78	11566	437	E	N	1	Y	
2012 Sep 16	22:05	A5	N18 W70	N-AR	244	E	N	1	N	
2012 Sep 25	04:24	C3.6	N09 E20	11577	465	SE	N	1	Y	B	...	
2012 Sep 27	22:36	C3.7	N09 W34	11575	344	SE	N	3	Y	A	...	
2012 Nov 8	02:08	M1.7	N14 E82	11611	Limb	
2012 Nov 10	04:22	C2.0	S25 E10	11608	637	E	N	2	Y	B	...	
2012 Nov 18	03:55	C5.7	N08 W22	11615	496	SW	N	2	N	A	...	
2012 Nov 20	19:21	M1.6	N05 E16	11618	422	SE	N	1	N	B	...	
2012 Nov 21	06:45	M1.4	N05 E11	11618	499	S	D	2	Y	B	...	
2012 Nov 21	15:10	M3.5	N05 E06	11618	778	E	B	3	Y	B	...	
2012 Nov 24	13:33	C3.3	N08 W29	11618	539	S	N	1	Y	A	...	
2012 Dec 5	00:12	C1.7	N17 E76	11628	681	SW	N	2	N	
2012 Dec 7	09:02	B4.8	N18 W78	11621	Limb	
2012 Dec 7	21:13	C3.9	N15 W73	11621	Limb	
2013 Jan 4	08:22	C1.3	S17 W34	11639	502	NE	N	2	N	A	...	
2013 Jan 5	16:19	C1.7	S13 W26	11645	507	SW	N	1	N	A	...	
2013 Jan 6	06:20	C8.4	S16 W52	N-AR	475	N	N	1	N	A	...	
2013 Jan 9	14:37	C3.1	N30 W105	11640	Limb	
2013 Jan 11	08:43	M1.2	N05 E36	11654	768	SW	D	1	Y	B	...	
2013 Jan 12	06:10	...	S13 W115	...	Limb	
2013 Jan 13	08:35	M1.7	N18 W22	11652	747	N	N	1	Y	A	...	
2013 Jan 18	16:50	C5.8	N12 E30	N-AR	529	W	N	1	Y	B	...	

^aN: No clear front, D: Dark front, B: Bright front

^b(1) Asai et al. (2012); (2) Chen & Wu (2011); (3) Chen et al. (2011); (4) Cheng et al. (2012); (5) Dai et al. (2012); (6) Downs et al. (2012);

(7) Gopalswamy et al. (2012); (8) Gopalswamy et al. (2013); (9) Gosain & Foullon (2012); (10) Harra et al. (2011); (11) Kozarev et al. (2011); (12) Kumar & Manoharan (2013); (13) Kumar et al. (2013); (14) Li et al. (2012); (15) Liu et al. (2010); (16) Liu et al. (2011); (17) Liu et al. (2012); (18) Long et al. (2011b); (19) Ma et al. (2011); (20) Olmedo et al. (2012); (21) Patsourakos et al. (2010); (22) Schrijver et al. (2011); (23) Shen & Liu (2012a); (24) Shen & Liu (2012b); (25) Shen & Liu (2012c); (26) Veronig et al. (2011); (27) Zheng et al. (2012a); (28) Zheng et al. (2012b)

Table 2. Number of LCPFs included in the present study, divided into different associations

Flare class	CME level				Type II burst		171 Å front		
	1	2	3	4	No	Yes	Not clear	Dark	Bright
X (11)	0	0	8	3	1	10	3	4	4
M (57)	13	14	25	5	19	38	20	25	12
C (49)	22	19	8	0	28	21	24	20	5
<C (21)	13	6	2	0	15	6	11	8	2